Draft version March 11, 2019
Preprint typeset using LaTeX style emulateapj v. 12/16/11

THE SPECTRAL EVOLUTION OF AT 2018DYB AND THE PRESENCE OF METAL LINES IN TIDAL DISRUPTION EVENTS

Giorgos Leloudas[1], Lixin Dai[2,3], Iair Arcavi[4], Paul M. Vreeswijk[5], Brenna Mockler[6,3], Rupak Roy[7], Daniele B. Malesani[8,3], Steve Schulze[9], Thomas Wevers[10], Morgan Fraser[11], Enrico Ramirez-Ruiz[6,3], Katie Auchettl[3], Jamison Burke[12,13], Giacomo Cannizzaro[5,14], Panos Charalampopoulos[3], Ting-Wan Chen[15], Aleksandar Cikota[16], Massimo Della Valle[17], Lluis Galbany[18], Mariusz Gromadzki[19], Kasper E. Heintz[20], Daichi Hiramatsu[12,13], Peter G. Jonker[5,14], Zuzanna Kostrzewa-Rutkowska[5,14], Kate Maguire[21,22], Ilya Mandel[23,24], Francesca Onori[25], Nathaniel Roth[26], Stephen J. Smartt[21], Lukasz Wyrzykowski[19], Dave R. Young[21]

Draft version March 11, 2019

ABSTRACT

We present light curves and spectra of the tidal disruption event (TDE) ASASSN-18pg / AT 2018dyb spanning a period of seven months. The event shows a plethora of strong emission lines, including the Balmer series, He II, He I and metal lines of O III λ3760 and N III $\lambda\lambda$ 4100 and 4640 (blended with He II). The latter lines are consistent with originating from the Bowen fluorescence mechanism. By analyzing literature spectra of past events, we conclude that these lines are common in TDEs. The spectral diversity of optical TDEs is thus larger than previously thought and includes N-rich besides H- and He-rich events. We study how the spectral lines evolve with time, by means of their width, relative strength and velocity offsets. The velocity width of the lines starts at $\sim 12\,000$ km s^{-1} and decreases with time. The ratio of Hα to Hβ remains close to three, while the ratio of He II over N III increases with time. The same is true for ASASSN-14li, which has a very similar spectrum to AT 2018dyb but its lines are narrower by a factor of >2. The emission lines start by being blueshifted by 800 km s^{-1} and move progressively to the red. High-resolution spectroscopy at maximum light does not reveal any narrow features that can be attributed to the TDE. By modeling the host galaxy spectral energy distribution, we obtain a stellar mass of $\log_{10}(M_\star/M_\odot) = 10.08^{+0.25}_{-0.24}$ and we quantify the degree of host contribution at different phases. By fitting the light curves of AT 2018dyb we estimate a mass of $4^{+5}_{-2} \times 10^6 M_\odot$ for the black hole and of $0.7^{+4}_{-0.6} M_\odot$ for the disrupted star. The detection of strong Bowen lines in the optical spectrum is an indirect proof for extreme ultraviolet and (re-processed) X-ray radiation and favors an accretion origin for the TDE optical luminosity. A model where photons escape after multiple scatterings through a super-Eddington thick disk and its optically-thick wind, viewed at an angle close to the disk plane, is consistent with the observations.

Keywords: Black hole physics – Galaxies: nuclei – Galaxies: individual: ASASSN-18pg, AT 2018dyb

[1] DTU Space, National Space Institute, Technical University of Denmark, Elektrovej 327, 2800 Kgs. Lyngby, Denmark
[2] Department of Physics, The University of Hong Kong, Pokfulam Road, Hong Kong
[3] Dark Cosmology Centre, Niels Bohr Institute, University of Copenhagen, Juliane Maries vej 30, 2100 Copenhagen, Denmark
[4] The School of Physics and Astronomy, Tel Aviv University, Tel Aviv 69978, Israel
[5] Department of Astrophysics/IMAPP, Radboud University Nijmegen, P.O. Box 9010, 6500 GL Nijmegen, The Netherlands
[6] Department of Astronomy and Astrophysics, University of California, Santa Cruz, CA 95064, USA
[7] The Inter-University Centre for Astronomy and Astrophysics, Ganeshkhind, Pune - 411007, India
[8] Cosmic DAWN centre, Niels Bohr Institute, University of Copenhagen, Juliane Maries vej 30, 2100 Copenhagen, Denmark
[9] Department of Particle Physics and Astrophysics, Weizmann Institute of Science, Rehovot 7610001, Israel
[10] Institute of Astronomy, Madingley Road, Cambridge CB3 0HA, United Kingdom
[11] School of Physics, OBrien Centre for Science North, University College Dublin, Belfield, Dublin 4, Ireland
[12] Department of Physics, University of California, Santa Barbara, CA 93106-9530, USA
[13] Las Cumbres Observatory, 6740 Cortona Dr Ste 102, Goleta, CA 93117-5575, USA
[14] SRON, Netherlands Institute for Space Research, Sorbonnelaan 2, 3584 CA, Utrecht, The Netherlands
[15] Max-Planck-Institut für extraterrestrische Physik, Giessenbachstraße, 85748 Garching, Germany
[16] Physics Division, Lawrence Berkeley National Laboratory, 1 Cyclotron Road, Berkeley, CA 94720, USA
[17] Ist. Nazionale di Astrofisica, Osservatorio Astronomico di Capodimonte (OACN), 80131 Napoli, Italy
[18] PITT PACC, Department of Physics and Astronomy, University of Pittsburgh, Pittsburgh, PA 15260, USA
[19] Warsaw University Astronomical Observatory, Al. Ujazdowskie 4, 00-478, Warszawa, Poland
[20] Centre for Astrophysics and Cosmology, Science Institute, University of Iceland, Dunhagi 5, 107, Reykjavik, Iceland
[21] Astrophysics Research Centre, School of Mathematics and Physics, Queen's University Belfast, Belfast BT7 1NN, UK
[22] School of Physics, Trinity College Dublin, Dublin 2, Ireland
[23] Monash Centre for Astrophysics, School of Physics and Astronomy, Monash University, Clayton, Victoria 3800, Australia
[24] Birmingham Institute for Gravitational Wave Astronomy, University of Birmingham, Birmingham, B15 2TT, UK
[25] Istituto di Astrofisica e Planetologia Spaziali (INAF), Via Fosso del Cavaliere 100, Roma, I-00133, Italy
[26] Department of Astronomy and Joint Space-Science Institute, University of Maryland, College Park, MD 20742, USA

1. INTRODUCTION

The optical spectra of tidal disruption events (TDEs) (Rees 1988) are usually assumed to be dominated by H and He lines (Arcavi et al. 2014). The large diversity in the ratio of H to He has been the topic of much discussion and has deep physical implications both for the nature of the disrupted star and the radiative processes taking place during the event (Gezari et al. 2012; Guillochon et al. 2014; Roth et al. 2016; Roth & Kasen 2018).

On the other hand, metal lines are prominent in the UV spectra of TDEs (Cenko et al. 2016; Brown et al. 2018) with the most notable being those of highly-ionized N, pointing to a possible relation to N-rich quasars (Kochanek 2016a; Liu et al. 2018). This raises the question of why such metal lines have not been unambiguously identified and reported in the optical regime. Indeed, Brown et al. (2018) speculate that, based on the UV spectra, the lines on the blue side of He II could be due to N III and C III similar to features seen in Wolf-Rayet stars. Recently, Blagorodnova et al. (2018) reported the detection of O III and N III lines in the spectrum of the TDE iPTF15af and attributed them to the mechanism of Bowen fluorescence.

The Bowen fluorescence mechanism (Bowen 1934, 1935) has been proposed and widely discussed to explain the prominent O III and N III optical emission lines observed in various and diverse astrophysical systems such as planetary nebulae (e.g., Unno 1955; Weymann & Williams 1969), X-ray binary stars (e.g., McClintock et al. 1975), and Wolf-Rayet stars (e.g., Crowther 2007). It has also been proposed in the context of supermassive black hole accretion disks by Netzer et al. (1985), but only recently identified in a flaring AGN for the first time (Trakhtenbrot et al. 2019). Since elements heavier than H and He should be rare in these systems, the only plausible explanation to see strong O III and N III fluorescent lines is that these lines are excited by some large sources of energy not available to the predominant H and He. In this mechanism, the eventual O III and N III optical emission features result from a series of processes. The first process is the ionization of singly ionized He (He II) by photons with wavelength shorter than 228 Å. During the recombination process of fully ionized He II, while the transition of one electron between the outer orbits can give rise to the optical lines such as He II at λ4686, the last transition from $n = 2$ to $n = 1$ produces an extreme ultra-violet (EUV) line at 304 Å. A secondary process is the excitation of a few O III and N III lines by the absorption of the intense EUV photons at 304 Å, because these ions have a transition very close to this wavelength by coincidence. These excited ions then return to the ground state through a series of transitions, producing optical lines such as O III at $\lambda\lambda$ 3047, 3133, 3312, 3341, 3444, 3760 and N III at $\lambda\lambda$ 4097, 4104, 4379, 4634 and 4641 (Osterbrock 1974).

In this paper we present observations of the newly discovered TDE ASASSN-18pg / AT 2018dyb which shows strong Bowen fluorescent N and O lines. At the same time, we revisit the spectra of past TDEs and we show that similar lines are conspicuous in many of them. Our data are presented in Section 2. The spectral evolution is described in Section 3 and we focus on the analysis of the emission lines in Section 4. Section 5 focuses on high-resolution spectroscopy. In Section 6 we examine the host galaxy properties and address the issue of host contamination, while in Section 7 we model the light curves to extract fundamental properties of the TDE and its progenitor system. Section 8 contains our discussion and Section 9 summarizes our conclusions.

2. OBSERVATIONS

ASASSN-18pg / AT 2018dyb was discovered by the All-Sky Automated Survey for Supernovae (ASAS-SN; Shappee et al. 2014) on 2018 July 11 (first detection at $V = 16.5$ mag), with the last non-detection ($V > 17.5$ mag) being nine days earlier (Brimacombe et al. 2018). It was classified as a TDE by Pan et al. (2018) on 2018 July 17, based on a spectrum obtained at the SOAR telescope. Our own observations set the precise redshift to $z = 0.0180$ (see Section 5), which is used throughout this paper. From now on we exclusively refer to AT 2018dyb with its official IAU name.

2.1. *Archival host galaxy observations and constraints on the nuclear nature of AT 2018dyb*

The location of AT 2018dyb was observed by the SkyMapper survey in 2015 (Wolf et al. 2018). We retrieved the SkyMapper images [27], and the host galaxy is detected in the *ugriz* filters (only marginally in *u*). It is also detected in the 2MASS survey, although blended with a nearby star of similar brightness.

The archival host detection allows to put constraints on the offset between host and transient. To measure the position of AT 2018dyb, we used a UVOT image in the UVW2 filter, taken close to maximum light (see Sect. 2.2), as there is negligible host contribution in the UV bands around that epoch. We measure RA = $16^{\rm h}10^{\rm m}58\overset{\rm s}{.}86$, Dec = $-60°55'24\overset{''}{.}28$ for the transient, calibrated against the Gaia survey catalog (we note that our position is $\approx 1.3''$ away from the one reported by Brimacombe et al. 2018). To accurately compute the offset, we cross-registered the UVOT and the SkyMapper images, which results in an RMS scatter of $\approx 0.25''$ in both RA and Dec, based on 26 common sources. This rather large scatter stems from the fairly wide PSF of the SkyMapper images ($\approx 2.5 - 3''$). For the host galaxy we measure RA = $16^{\rm h}10^{\rm m}58\overset{\rm s}{.}89$, Dec = $-60°55'24\overset{''}{.}46$, i.e. an offset of $0\overset{''}{.}21$ in RA and $0\overset{''}{.}18$ in Dec. The transient is thus consistent with the location of the nucleus within our measurement uncertainties. For reference, at $z = 0.0180$, $0.25''$ corresponds to 100 pc.

2.2. *UVOT photometry*

Photometry of AT 2018dyb was obtained by the Neil Gehrels *Swift* Observatory between 2018-07-18 and 2019-02-18 in 28 epochs. The transient was bright in all near-UV (NUV) and optical filters of the *Swift*/UVOT telescope. The UVOT data were reduced using the standard pipeline available in the HEAsoft software package [28]. Observation of every epoch was conducted using one or several orbits. To improve the S/N ratio of the observation in a given band in a particular epoch, we co-added all orbit-data for that corresponding epoch using

[27] `http://skymapper.anu.edu.au/`
[28] `https://heasarc.nasa.gov/lheasoft/`

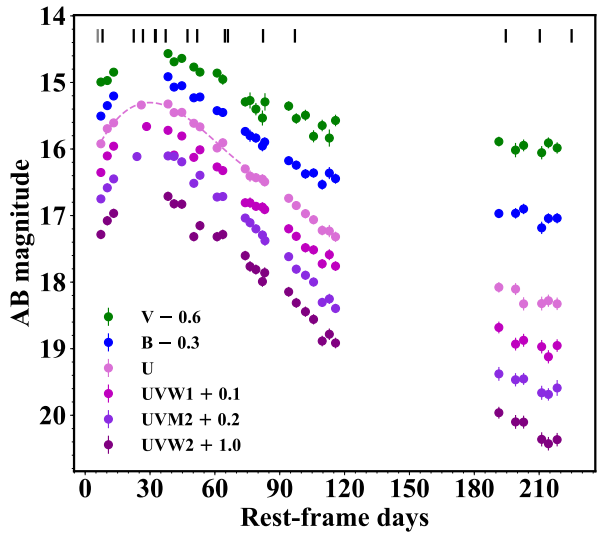

Figure 1. The UVOT light curves of AT 2018dyb shown in rest-frame days with respect to the discovery date MJD = 58310.23 (Brimacombe et al. 2018). The light curves are shifted for clarity as indicated in the legend. Vertical bars denote epochs of spectroscopic observations. A polynomial fit on the U-band light curve shows that maximum light occurred 30.0±2.6 rest-frame days after discovery.

the HEAsoft routine `uvotimsum`. We used the routine `uvotdetect` to determine the correct position of the transient (which is consistent with the ground-based optical observations) and used the routine `uvotsource` to measure the apparent magnitude of the transient by performing aperture photometry. As late time images reveal the presence of multiple contaminating sources near the transient and its host, for source extraction we used a small aperture with a radius 3″ while an aperture of radius 100″ was used to determine the background. Our photometry is listed in Table 1 and on the AB system. The light curves of AT 2018dyb are shown in Figure 1. Our reference time is the date of discovery MJD = 58310.23 (Brimacombe et al. 2018). Maximum light in the U-band occurred at MJD = 58340.74 (Figure 1). We note that the UVOT photometry is not host subtracted. This is further discussed in Section 6.

2.3. *Las Cumbres and ePESSTO spectroscopy*

We have collected low-resolution spectra of AT 2018dyb using the FLOYDS instrument on the Las Cumbres Observatory [29] (LCO) 2-meter telescope in Siding Spring, Australia (Brown et al. 2013) and with EFOSC2 on the New Technology Telescope (NTT) in La Silla Observatory, Chile, as part of the ePESSTO survey (Smartt et al. 2015). The LCO spectra were reduced using the pyraf-based `floydsspec` pipeline originally developed by S. Valenti. The NTT spectra were reduced in a standard manner with the aid of the PESSTO pipeline (Smartt et al. 2015). A spectroscopic log can be found in Table 2 and the spectral series is shown in Figure 2. All spectra will be available [30] through the WISeREP archive (Yaron & Gal-Yam 2012).

[29] `http://lco.global`
[30] after acceptance of the paper

2.4. *UVES spectroscopy*

In addition, we obtained high-resolution spectroscopy with the Ultraviolet and Visual Echelle Spectrograph (UVES) mounted on the Kueyen unit of ESO's Very Large Telescope (VLT). AT 2018dyb was observed on the nights of 2018 July 22, 23 and August 16. The dichroic/central wavelength settings 346+580nm (dichroic 1) and 437+860nm (dichroic 2) were used, covering the full optical range 305-1040 nm, with the exception of small gaps at 575.5-583.8 nm and 851.7-867.4 nm, in two exposures. During the night of July 22, only a single setting (346+580nm) could be obtained through thick cirrus before the telescope had to be closed. The data were reduced with the UVES pipeline (Ballester et al. 2000) and the spectral trace, wavelength calibration solution and final extraction were inspected and slightly improved by adjusting some of the pipeline recipe parameters. The r.m.s. of the wavelength solution varied between 0.001 and 0.005 Å. The incomplete data from July 22 were co-added with the data from July 23 to produce a single spectrum covering the whole wavelength range.

2.5. *X-rays*

We finally note that AT 2018dyb does not exhibit strong X-rays. Using the *Swift* XRT observation at time of discovery, Miller & Cenko (2018) derived a conservative upper limit to the absorbed flux of 7×10^{-14} erg cm^{-2} s^{-1} (0.003 counts s^{-1}) in the 0.3–10.0 keV band, assuming a blackbody with a kT = 0.2 keV. By merging the first 14 epochs of the Swift XRT observations, we derive a slightly lower upper limit of 1.6×10^{-3} counts s^{-1}. Using a blackbody model with kT = 0.2 keV and a Galactic column density of $N_{\rm H} \sim 1.83 \times 10^{21}$ cm^{-2}, we derive an upper limit for the absorbed flux of 3.4×10^{-14} erg cm^{-2} s^{-1}. This corresponds to an unabsorbed flux of 7.8×10^{-14} erg cm^{-2} s^{-1} and, at the redshift of the host, to a luminosity of $\sim 5.6 \times 10^{40}$ erg s^{-1}, which suggests no evidence of a strong AGN (e.g., Tozzi et al. 2006; Liu et al. 2017; Ricci et al. 2017).

3. SPECTRAL EVOLUTION

The first spectra of AT 2018dyb are dominated by Hα and three more broad features centered at 4660, 4100 and 3760 Å. At these phases, Hβ is weak and Hγ is not detected, providing the first evidence that the line at 4100 Å is unlikely to be Hδ as previously identified in TDEs with similar spectra (e.g. Holoien et al. 2016b; Hung et al. 2017). As time evolves, the spectrum becomes redder and the lines become narrower. At the same time, Hβ and Hγ emerge and become stronger with time, but remain always weaker than the 4100 Å line. We propose here that this strong line is dominated by N III λ4100 (blend of $\lambda\lambda$4097, 4103). In addition, we identify the bluer broad feature as O III $\lambda\lambda$ 3754, 3757 and 3759, a blend of the strongest O III lines in the optical (National Institute of Standards and Technology, Atomic Spectra Database Lines Data; Kramida et al. 2015), which from now on we will call O III λ3760 for simplicity. The simultaneous detection of these N III and O III lines is compatible with the idea that they might originate from Bowen fluorescence (Blagorodnova et al. 2018; Trakht-

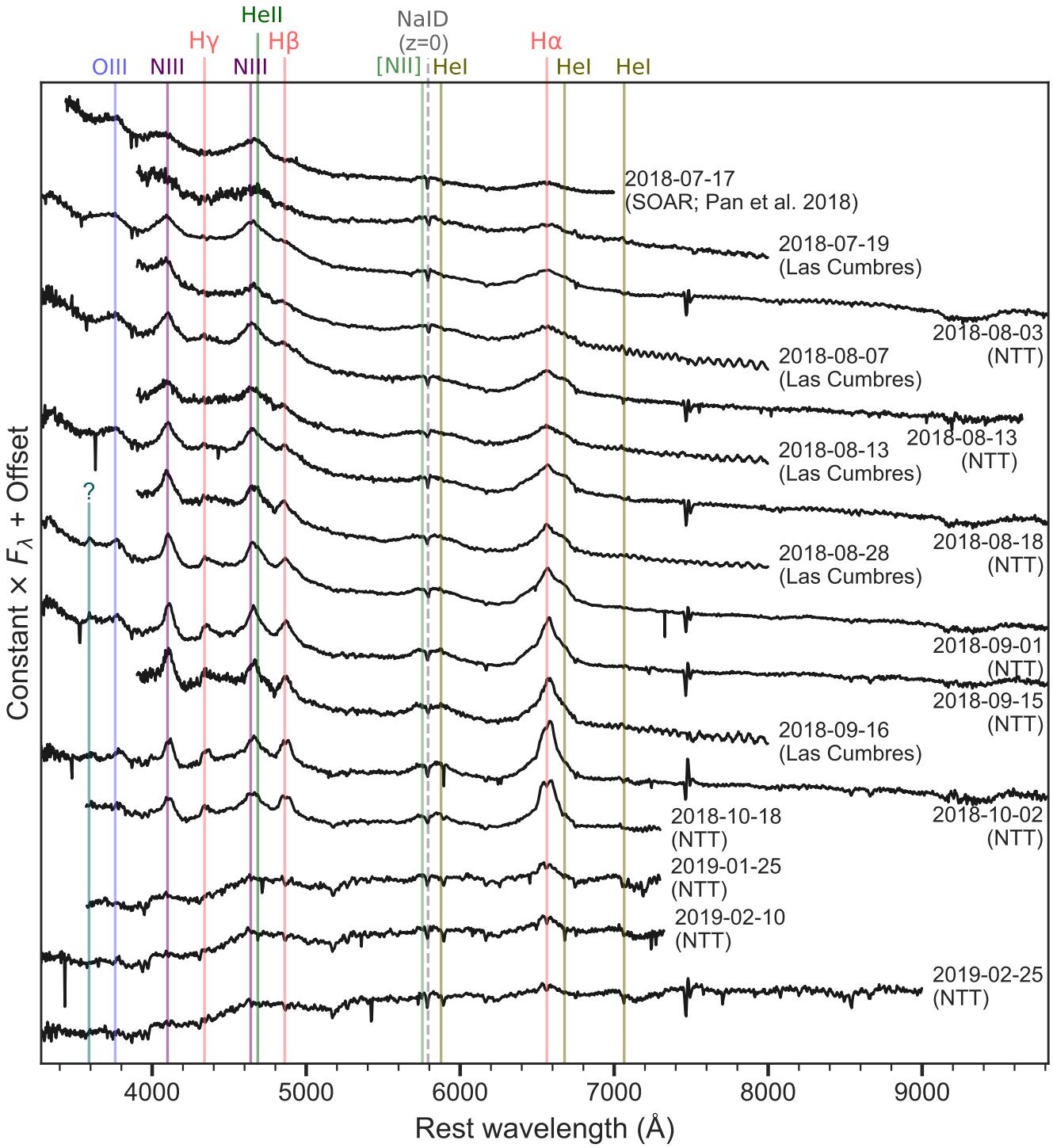

Figure 2. The low resolution spectra of AT 2018dyb with the strongest broad lines identified. The SOAR spectrum (Pan et al. 2018) has been retrieved from the Transient Name Server.

enbrot et al. 2019) and strengthens these identifications (as these lines are expected to appear together due to the same physical mechanism). In addition, this identification suggests that the broad line at 4660 Å is (at least partially) due to N III λ4640 and not (exclusively) He II λ4686, as usually assumed.

Together with the emergence of Hβ and Hγ we have the appearance of a shoulder in the red wing of Hα, which can be attributed to He I λ6678. This raises the question of whether the last strong feature apparent in the optical spectrum, between 5690 and 5890 Å, can be due to He I λ5876. It is unlikely that this is the sole contribution to this feature, given that He I would need to be blueshifted by 5000 km s^{-1}, while the other lines in the spectrum appear close to rest velocity. Blagorodnova et al. (2018) suggested an alternative identification for this line as [N II] λ5754, but this association is not secure either. We stress that the profile of this line is

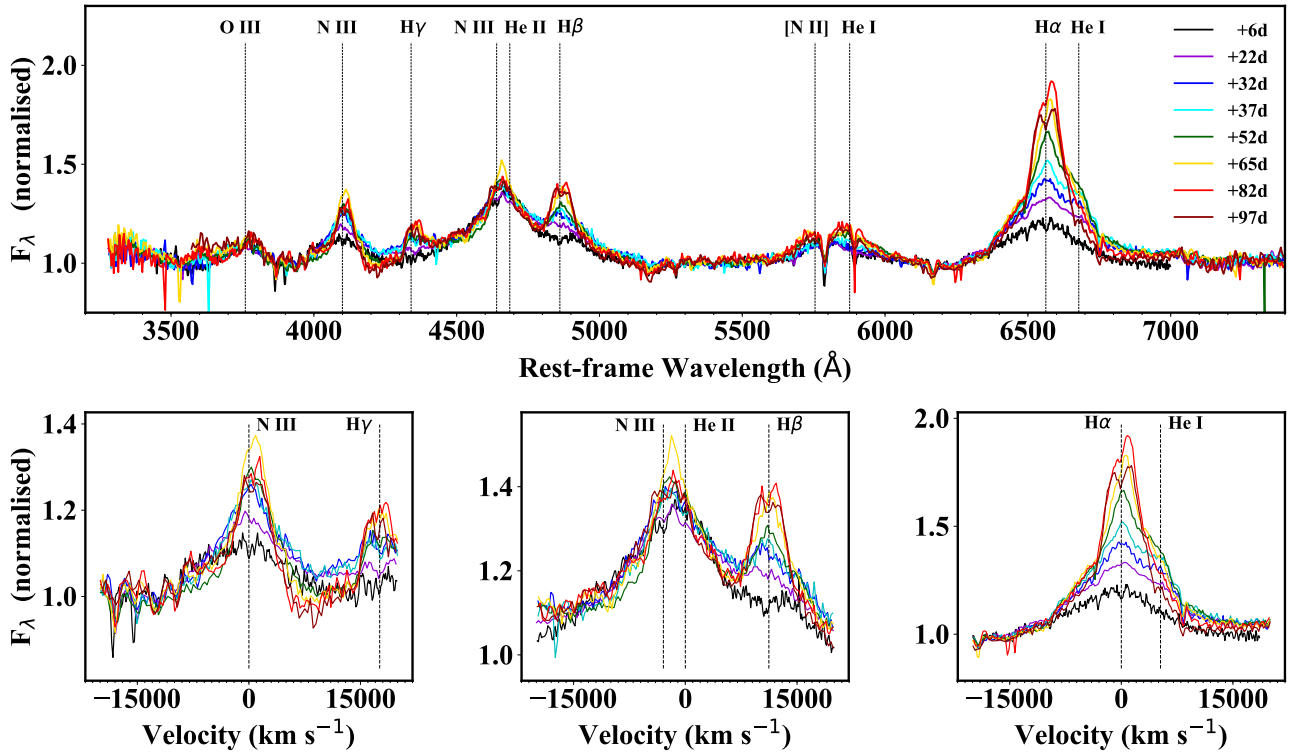

Figure 3. Upper panel: Selected spectra of AT 2018dyb after normalising with the continuum, over-plotted with different colors as indicated in the legend. The phases refer to the time of discovery and they are given in the rest frame. The strongest lines have been identified. All lines grow stronger with time and this is particularly true for the Balmer lines. **Lower panels:** A zoom in some of the strongest lines in velocity space. In the middle panel, the zero velocity has been set considering He II, but it can be seen that the line peaks between He II and N III and that the line is likely a blend. The width of the lines starts at ∼12,000 km s^{-1} and decreases with time (see also Figure 5).

complicated and it is strongly affected by strong Galactic Na I D absorption. So we tentatively identify this feature as a blend of the above lines. Finally, one feature remains unidentified, a weak line at 3590 Å which appeared after September 1 to the blue of the O III blend.

AT 2018dyb disappeared behind the Sun around mid October 2018. The first spectrum after it re-appeared in January 2019, shows that most features have weakened or disappeared in the meantime. The spectrum resembles mostly that of an elliptical galaxy with a superimposed broad Hα component, due to the TDE, and some residual flux at the N III/He II region, although individual broad features can no longer be clearly identified there. At the same time, the TDE has faded by more than 1 mag in the UV bands.

4. EMISSION LINE ANALYSIS

In order to focus on the emission lines, we have first de-reddened and then removed the continuum from the spectra. The spectra were de-reddened for the Galactic extinction towards the direction of AT 2018dyb of $A_V = 0.625$ mag (Schlafly & Finkbeiner 2011), while no extinction was assumed for the (passive) host galaxy. These choices are discussed further below. Subsequently, we fit a low-order polynomial in the regions of the spectra that we estimated were continuum dominated. While this procedure is subjective to some degree, it is standard practice in the literature. As the AT 2018dyb spectra have not been host subtracted, we stress that this procedure removes the total continuum (TDE+host) and could leave some line contamination from the host. However, inspecting the last spectra obtained after January, we estimate that this line contamination is small. This analysis was only attempted in the 'early' spectra (up to 100 days past discovery and before the TDE disappeared behind the Sun in mid-October).

By dividing with the continuum we obtain the normalised spectra that can be seen in Figure 3. In this figure it is immediately apparent that the emission lines grow stronger with time with respect to the continuum (their equivalent width gets larger). The lower panels zoom in the strongest features and show their evolution in velocity space. The FWHM of the lines is approximately ∼12,000 km s^{-1} at discovery and decreases with time. In the last two spectra, an absorption component becomes visible in the middle of the Hα and Hβ lines (at $v = 0$ km s^{-1}). This is a host galaxy feature (stellar absorption) that becomes relatively more important as the host galaxy contribution increases with time. However, these features are weak compared to other TDEs where they dominate the spectrum even at maximum light (e.g. Holoien et al. 2016b; Blagorodnova et al. 2017). This is due to the fact that the host of AT 2018dyb is not an E+A galaxy as has been observed for many TDEs (Arcavi et al. 2014; French et al. 2016).

Figure 4 shows a comparison of AT 2018dyb with other TDEs. The top spectra (blue) are 'He-rich' with no evidence for H lines or other strong features. In addition, the broad He II line of ASASSN-15oi (Holoien et al. 2016a) appears clearly blueshifted, while for PS1-10jh it appears almost at rest velocity, albeit with a visible

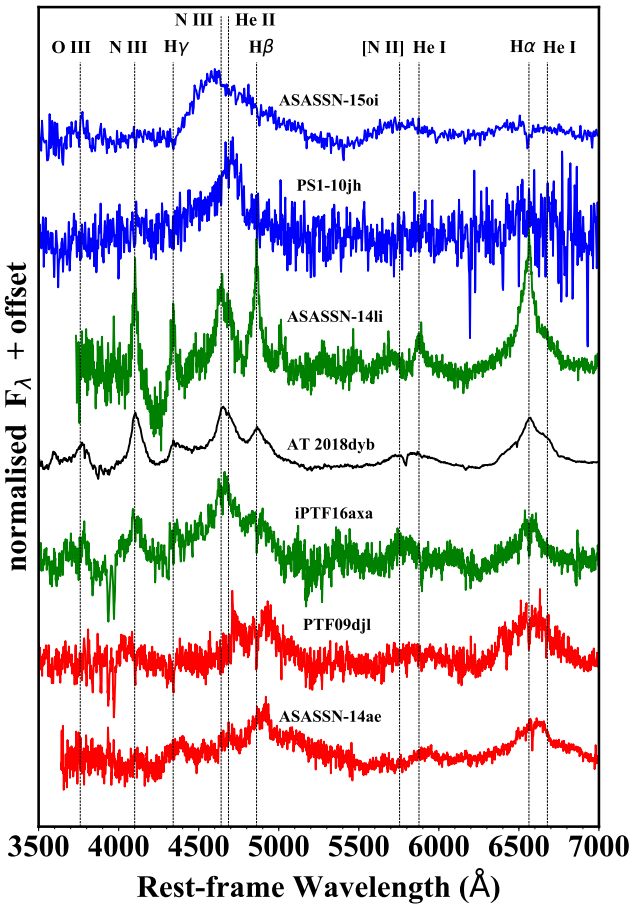

Figure 4. AT 2018dyb compared to other TDEs. This is a version of the original plot by Arcavi et al. (2014), where we focus on the existence of events with strong N and O lines ('N-rich'). The top spectra belong to two 'He-rich' events which do not show any evidence for H lines (Holoien et al. 2016a; Gezari et al. 2012). The next three spectra show TDEs that, in addition to He II, show a clear peak at 4640 Å and/or a very strong line at 4100 Å (both attributed to N III) and/or another emission line at ∼3760 Å (O III). The spectra of AT2018dyb and ASASSN-14li are very similar, but the lines of ASASSN-14li are narrower. Finally, the bottom two spectra (Arcavi et al. 2014; Holoien et al. 2014) show weak or absent He II (or N and O) lines, especially in comparison to their strong H lines.

blue wing (as also noted by Gezari et al. 2012). The bottom spectra (red) show weak or no He II lines, while the dominant features are Balmer lines (Arcavi et al. 2014; Holoien et al. 2014). AT 2018dyb is more similar to the middle (green) spectra (Holoien et al. 2016b; Hung et al. 2017) that show the following properties: a clear peak at 4640 Å and/or a very strong line at 4100 Å (both attributed to N III) and/or another emission line at ∼3760 Å, attributed to O III. We observe that the spectrum of AT 2018dyb is very similar to ASASSN-14li with the main difference being that the lines are narrower in ASASSN-14li. In fact, for this TDE, N III λ4640 and He II λ4686 are clearly resolved into two peaks confirming that i) the identification of N III is solid and ii) both lines are at zero velocity. iPTF16axa also has the same set of N and O lines and so does iPTF15af (Blagorodnova et al. 2018), showing that these metal lines are common in TDEs. A subset of TDEs are therefore 'N-rich'.

To get a quantitative view of the line evolution, we fit the emission lines with Gaussian profiles. This is done with custom made routines based on `mpfit` (Markwardt 2009). First, Hα is fit simultaneously with He I λ6678. In the blue part of the spectrum, where many lines are blended together, we fit five line simultaneously, namely the line at 4100 Å, Hγ, N III, He II and Hβ. This is a fit with many free parameters and we therefore impose some reasonable constraints in order to include some physical information and reduce the number of possible solutions. We require that Hβ and Hγ have similar FWHM with Hα (within 2000 km s^{-1}). Similarly, we constrain the FWHM of the two N III lines to be the same. We also allow only limited velocity shifts for the central wavelengths of the lines. For comparison, we fit the same set of lines in ASASSN-14li. In this case, the lines are narrower and resolved and it is not necessary to make a simultaneous fit for all five lines. It is enough to perform a double Gaussian fit to N III and He II and fit the other lines independently.

The upper panels of Figure 5 show the FWHM evolution of the emission lines. We observe that the Hα and the λ4100 line (assumed to be N III) have a similar evolution, starting from a width of 12 000 km s^{-1} five days after discovery and decreasing gradually to 6–7 000 km s^{-1} almost 90 days later. The width of the λ3760 line (O III) is similar at early times but the line profile evolves to become more complicated later and can no longer be fit by a single Gaussian. The line widths of ASASSN-14li also show a similar decreasing behavior (Holoien et al. 2016b) but they are substantially lower compared to AT 2018dyb, evolving from 6 000 to 2 000 km s^{-1}. This is why N III and He II can easily be resolved in this TDE, while a de-blending is needed for AT 2018dyb. Interestingly, in ASASSN-14li both N III $\lambda\lambda$ 4100, 4640 and He II seem to show an initial increase (for the first 30 days), which is not the case for the Balmer lines. We should note that while the error bars we present include a proper propagation of the error spectrum and the errors in the line fits (resulting from `mpfit`), they do not include any estimate for the uncertainty during the procedure of removing the continuum. This systematic error is likely the most dominant and thus the errors in Figure 5 are underestimated. However, the FWHM evolution in the de-blended He II line of AT 2018dyb also shows a similar evolution which indicates that this might be real.

The middle panels of Figure 5 show the evolution in several line ratios for the two TDEs. Absolute line luminosities are less reliable as they are more prone to uncertainties in the reddening correction. Nevertheless, we observe that the Hα/Hβ ratio remains close to three, both for AT 2018dyb and for ASASSN-14li. This value is sufficiently close to the value expected in case B recombination for zero extinction. This coincidence indicates that the assumption we made about the reddening correction should be close to real. Within the measurement precision (recalling that error bars shown are underestimated) there is some evidence that this ratio is increasing with time, which is reinforced by the latest observation of ASASSN-14li, where it has a value closer to six, albeit with significant uncertainty. The Hβ/Hγ ratio remains close to unity for AT 2018dyb. This is why we deem that it is very unlikely that the λ4100 line can

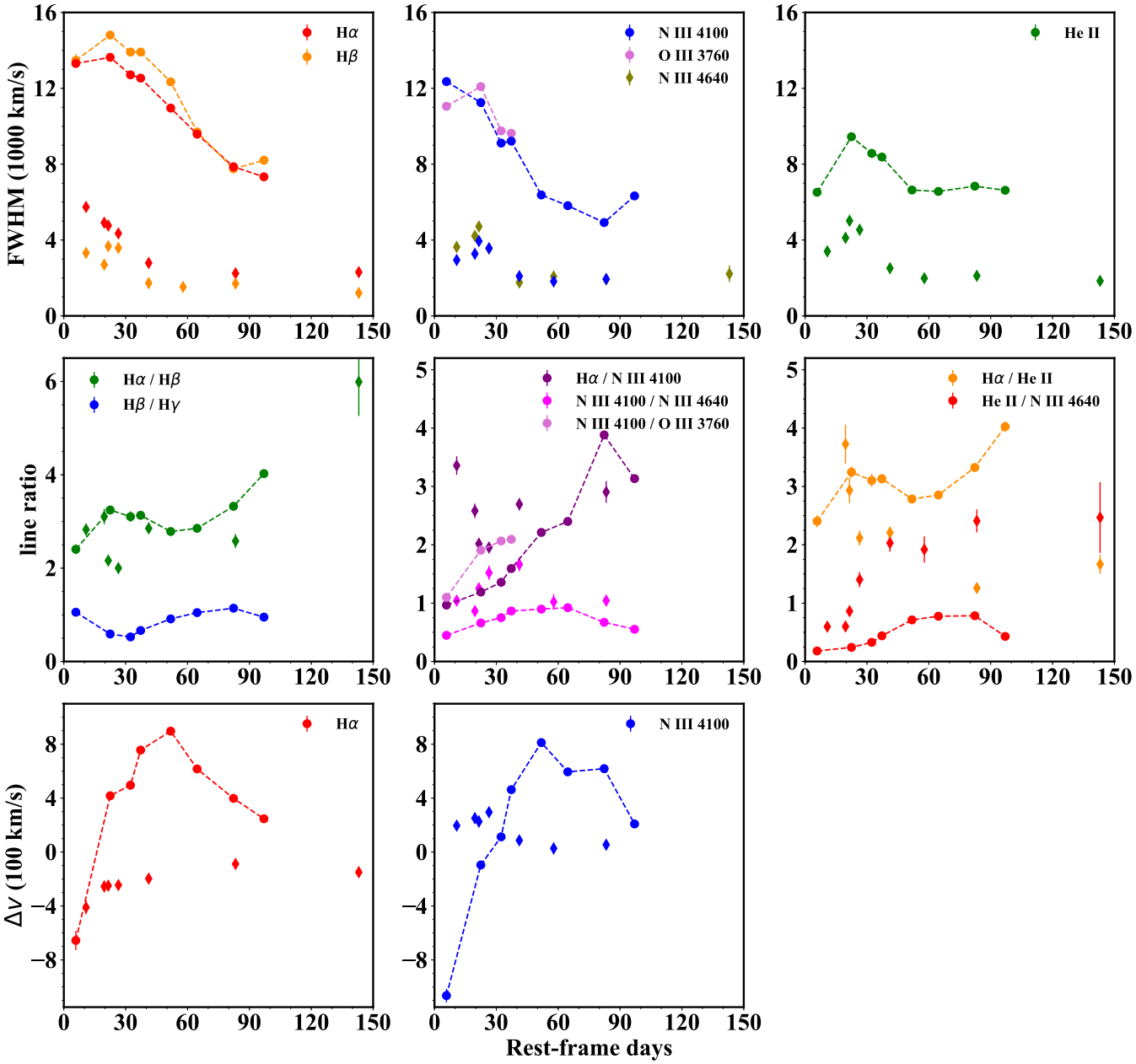

Figure 5. Evolution of line widths (upper panels), line ratios (middle panels), and velocity offsets (lower panels) for emission lines in the spectra of AT 2018dyb (circles connected with dashed lines) and ASASSN-14li (diamonds), with respect to the date of discovery. The color coding for each line (or line ratio) is explained in the legends.

be dominated by Hδ. The ratio of Hα/λ4100 (shown in the next panel) starts close to unity and increases with time until Hα becomes four times stronger. The ratio of the two N III lines evolves smoothly between 0.5 and unity, while the ratio of N III λ4100 to the O III blend at λ3760 also increases with time. Especially interesting is the ratio of He II/N III λ4640. For both AT 2018dyb and for ASASSN-14li, N III starts as the strongest line close to discovery. However, for both events this ratio increases with time and for ASASSN-14li (where this is also clearly seen by eye as the lines are resolved) it completely reverses 50 days later. We also show the ratio of Hα to He II (after removing the N III contribution). For AT 2018dyb this ratio is approximately equal to three and shows a possible increasing trend after 60 days.

Finally, in the lower panels of Figure 5 we show the velocity shifts of some lines with respect to their rest-frame velocity. We focus only on the Hα and the N III λ4100 which are the most isolated lines and give the most reliable results. For many other lines the exact shifts depend on the details of the (quintuple) line fit and/or are part of the fit constraints themselves. However, these two lines always give consistent results. It is very interesting that both lines start with a blueshift of 800-1 000 km s^{-1} but quickly shift to the red (again by 800 km s^{-1}) in a timescale of 50 days. Subsequently, their line centre seems to return again towards rest velocity. ASASSN-14li also shows evidence for an initial blueshift evolving to rest velocity in Hα, although this is less prominent (400 km s^{-1}) and it is not confirmed by the λ4100 line.

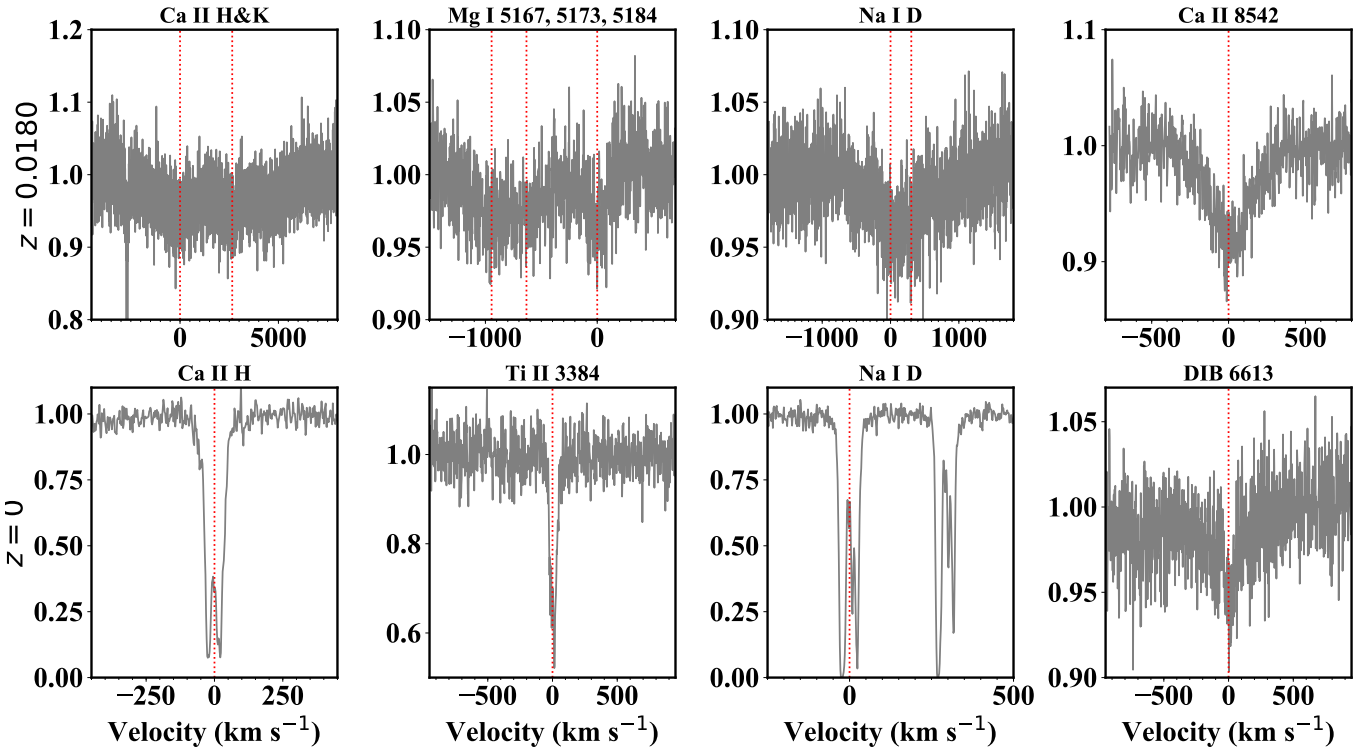

Figure 6. A selection of narrow features from the UVES spectra, plotted in velocity space. The top panels show features at the host galaxy of AT 2018dyb, while the bottom panels show features at $z = 0$.

5. HIGH RESOLUTION SPECTROSCOPY

We have used our UVES spectroscopy to search for narrow (of the order of 10–100 km s^{-1}) absorption features in the spectra. We identify two kinds of lines: i) absorption and diffuse interstellar bands (DIBs) in the Milky Way at $z = 0$ (the Na I $\lambda\lambda$3302, 3303 UV doublet, Na I D, a couple of Ti II transitions, Ca II H&K, and several DIBs at 6196, 6204, 6284 and 6613 Å); ii) lines originating at the host galaxy (Ca II H&K, Mg I $\lambda\lambda$5167, 5173, 5184, Na I D and two Ca II lines in the NIR - the third falls in the UVES red CCD chip gap). Apart from these features, we do not detect any other line. In particular, we do not detect any line that we can attribute to the TDE itself, e.g. narrow blueshifted lines or P-cygni absorption profiles that could be indicative of winds or outflowing material. A selection of narrow features from the UVES spectra are shown in Figure 6.

We have fit the NIR Ca II lines to derive a redshift for the host of $z = 0.0180$. These lines are not 'narrow' but have width of a few hundred km s^{-1}. In particular, we get a FWHM of $\sim$ 290 km s^{-1} for both Ca NIR lines (fit simultaneously) for both epochs. This indicates that they are not ISM lines but stellar features at the host. Blagorodnova et al. (2017) used these lines to calculate the velocity dispersion at the host of iPTF16fnl and from there the mass of the supermassive black hole. Following the same procedure and the $M - \sigma$ calibration of McConnell & Ma (2013), we obtain $\sim 1.4 \times 10^7 M_\odot$ for AT 2018dyb. However, Wevers et al. (2017) showed that an estimate based solely on these lines, can give different results than a full template fitting for the determination of σ, probably because these lines can get collisionally broadened. So we do not consider this value to be reliable. The other host lines are quite shallower but a forced fit on the Na I D lines gives a similar width of 266 ± 22 km s^{-1}. The host Ca II H&K lines are more difficult to study as they are in a region with many strong TDE lines and the continuum determination is more ambiguous.

The Galactic Na I D lines have a complex profile with four components and equivalent widths of 1.01 Å for D1 and 0.78 Å for D2. However, the lines are saturated. In addition, we measure an equivalent width of 0.076 Å for the DIB at 6613 Å, which is the strongest and 'cleanest' among the DIBs detected. We note that the strength of these lines is perhaps larger than what is expected from the Galactic extinction towards this direction. By using a relation provided by Friedman et al. (2011), the measured 6613 Å DIB strength would correspond to $E(B-V) \sim 0.37$ mag, which is almost double from the $E(B-V) \sim 0.2$ mag obtained by the Schlafly & Finkbeiner (2011) maps. Nevertheless, these scaling relations are known to have significant scatter and we therefore adopt the Schlafly & Finkbeiner (2011) value.

6. HOST GALAXY AND HOST CONTAMINATION

There are two main reasons to study the host galaxy of AT 2018dyb. The first is that fundamental properties of the galaxy, such as the stellar mass and star formation rate (SFR), can be linked to the properties of the TDE progenitor system, i.e. the mass of the supermassive black hole (e.g. McConnell & Ma 2013) or the probable mass of the disrupted star (Kochanek 2016b). The second reason is that we are interested in placing constraints to the degree of host contamination on the light curves and spectra of AT 2018dyb.

To this end we modelled the host spectral energy distribution (SED) with the software package `LePhare`, ver-

sion 2.2 (Arnouts et al. 1999; Ilbert et al. 2006) [31]. For a detailed description of the SED modeling we refer to previous publications where a very similar procedure was used (Krühler et al. 2011; Leloudas et al. 2016; Schulze et al. 2018) and the references therein. As input, we used the archival *ugriz* data from SkyMapper and the *JHK* data from 2MASS. We performed photometry on equal seeing ($\sim$2.5″) images with a small aperture (3″) in order to avoid the contamination by neighbouring objects. However, due to the large seeing and relatively large pixel scales, this may not have been entirely possible. For this reason we experimented with different combinations of filters and apertures and studied how this affected the SED modeling. We conclude that the results that we report here are within the precision that we are interested in for the scope of this paper. More accurate results will be possible in the future, after the TDE has faded.

We obtain a total stellar mass of $\log_{10}(M_\star/M_\odot) = 10.08^{+0.25}_{-0.24}$ and a SFR of $6.48^{+22.83}_{-3.56}$ $M_\odot$ yr^{-1} (where the central value is the median of the probability distribution and the error bars contain the 1σ probability interval). The stellar mass is relatively robust and does not seem to depend on the exact choice of input, while the SFR is more uncertain and its value should be treated with caution. Using an empirical relation between the mass of the galaxy and the mass of the black hole (Reines & Volonteri 2015), we obtain $4.6^{+13.6}_{-3.4} \times 10^7 M_\odot$ for the black hole mass.

In addition, through the SED fit it is possible to obtain model magnitudes in the UVOT bands, including in the UV where archival observations do not exist. These are of course more uncertain than real observations but we deduce the following: i) the host contamination is negligible in the UV bands around maximum light; ii) the host contamination stays always below 5% for UVW2 and UVM2 and below 10% for the UVW1 filters for the first 120 days past discovery (conservative limit); iii) in the U band the contamination stays below 10% for the first 90 days while it increases to 20% at 120 days past discovery; iv) on the contrary, in the B and V bands the host contribution is never below 10% (except the three B band data points at maximum) and it becomes dominant as the TDE fades, as also demonstrated by the flattening of the light curves (Figure 1).

7. FITS TO THE LIGHT CURVE

By fitting a black body to the UVOT photometry of AT 2018dyb, we estimate the photospheric temperature, black-body radius and bolometric luminosity at different phases (Figure 7). We only fit data out to 120 days past discovery and we made two separate fits (after removal of our best estimate host contamination; Section 6): one including all UVOT data and one where we excluded the B and V data. In both cases, we get consistent results within the errors but there seems to be a systematic offset between the two estimates. The temperature considering the UV data alone is $\sim$ 3000 K higher, which indicates that the host contribution in the redder bands might have been underestimated. In any case, the temperature remains approximately constant around $\sim$ 25000 K (adopting the UV fit that is more reliable and with more conservative errors). In that sense, AT 2018dyb is similar

[31] http://www.cfht.hawaii.edu/~arnouts/LEPHARE/lephare.html

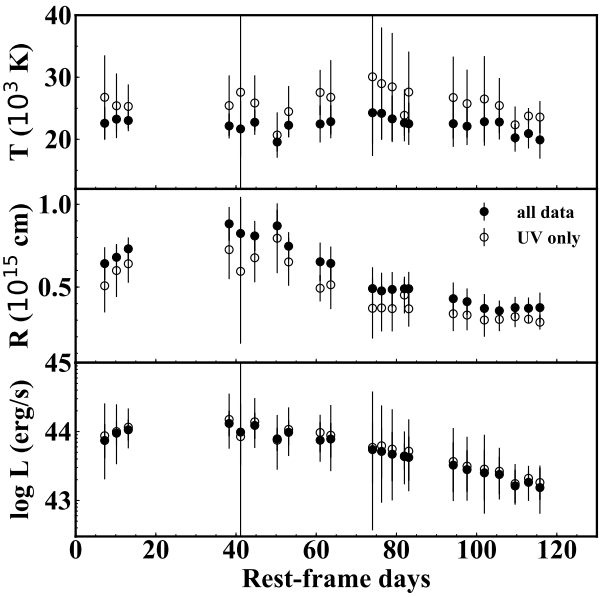

Figure 7. Evolution of temperature, radius and bolometric luminosity for AT 2018dyb, by fitting a black body to the UVOT photometry (after removal of the host contribution). We made two different fits, one including all UVOT data and one excluding the B and V bands. The temperature stays approximately constant during the first 120 days in both cases, although there is a small systematic offset between the two estimates.

to many other optical TDEs (e.g. Holoien et al. 2016b; Hung et al. 2017) although it is now documented that the temperature evolution of TDEs is quite diverse (Holoien et al. 2016a; Leloudas et al. 2016; Holoien et al. 2018).

We used the transient fitting code `MOSFiT` (Guillochon et al. 2017) to fit the light curves of AT 2018dyb. `MOSFiT` uses a library of tidal disruption simulations from Guillochon & Ramirez-Ruiz (2013) to calculate the mass fallback rate, and then scales the fallback rate using the properties of the black hole and disrupted star. It then converts the fallback rate into a bolometric luminosity curve and passes it through a viscous transform, approximating a viscous delay from an accretion disk or a diffusion delay through a dense photosphere. Finally, it uses a time-dependent reprocessing function to produce optical and UV light curves. The model is explained in detail in Mockler et al. (2019). The results of the code include best fit parameter estimates for the masses of the black hole and the disrupted star.

The fits obtained for AT 2018dyb can be seen in Figure 8. In this run we only fit data that is completely free of host contamination, i.e. only the bluest UV bands and only up to 90 days past discovery (see Section 6). The data have only been corrected for Galactic extinction. We find that the best fit for the black hole mass is $4^{+5}_{-2} \times 10^6 M_\odot$ (substantially lower than the estimate we derive from the host galaxy mass scaling relation) and the best fit for the star mass is $0.7^{+4}_{-0.6} M_\odot$. The fit preferred a full disruption of the star. The errorbars include $\pm$0.2 dex of systematic error in the black hole mass measurement, and $\pm$0.66 dex of systematic error in the stellar mass measurement.

We also ran a fit on preliminary host-subtracted data, and found that the best fit black hole mass did not change

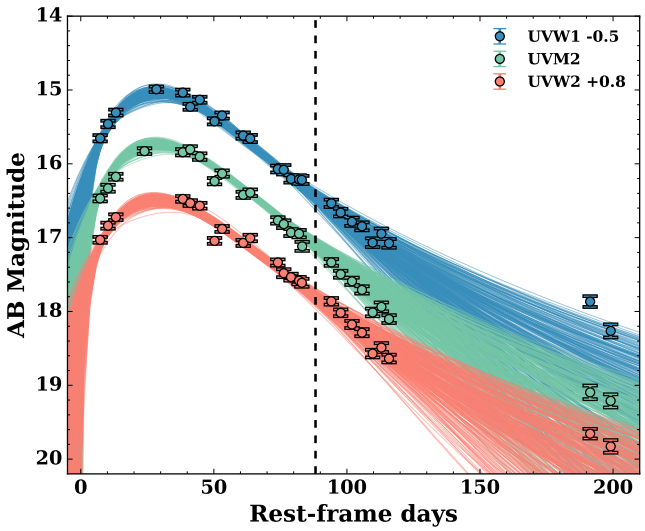

Figure 8. Best fit light curves from `MOSFiT`. The fit only used UV observations out to the dashed line at rest-frame day 88.2 (MJD = 58400). As shown in Section 6, host contamination is negligible for these data and all the light comes from the TDE. The light curves have been extrapolated out to later times for the plot.

significantly. However, the best fit star mass increased and the fit preferred a partial disruption instead of a full disruption. As the host-subtracted magnitudes are still uncertain (see section 6), we are not confident in the accuracy of this second fit. Therefore, for now we adopt the more conservative fit to the UV data.

8. DISCUSSION

The main observational result of this paper is the presence of strong N and O lines in the optical spectra of AT 2018dyb and the ascertainment that these lines are relatively common in optical TDEs.

TDEs can have N features due to its enhancement in the debris falling back at some phase after peak (Kochanek 2016a). This is especially the case for the disruption of more massive stars since their N abundance increases more dramatically over the main-sequence evolution (Gallegos-Garcia et al. 2018). However, the enhancement in the TDE debris fallback itself is not sufficient to explain the strong N line observed here with flux comparable with Hα and He II. For example, even for a massive star of mass $\sim 3M_{\odot}$ near the end of its main-sequence evolution, the fallback abundance of N can only be enhanced to 8 times of its solar abundance, still putting it at a ratio of $\sim 1:100$ compared with H. Furthermore, from the `MOSFiT` fit the disrupted star in AT 2018dyb is more likely to have a low mass, so the N enhancement over its lifetime should not be very significant. Therefore, we conclude that Bowen fluorescence is the most likely mechanism for producing the observed strong N III features by exciting N with energy unavailable to H and He.

It is reassuring that so far all TDEs with prominent Bowen features (AT 2018dyb, ASASSN 14-li, iPTF15af, iPTF16axa) are all accompanied by strong He II optical lines, since Bowen fluorescence is primarily triggered by the ionization and recombination of He II. The detection of O III lines further lends support to this mechanism. However, not all TDEs with He II lines have strong Bowen features, perhaps because they do not produce the optimal physical conditions (such as temperature, optical depth and velocity gradient) needed for strong resonance to happen (Weymann & Williams 1969; Kallman & McCray 1980; Selvelli et al. 2007). Interestingly, all of the hitherto identified N-rich TDEs also show Balmer emission besides He II. In addition, for both AT 2018dyb and ASASSN-14li, the ratio of N III to He II is observed to decrease with time. The exact ratio of the different emission lines and their evolution (Figure 5) can be used to shed light on the physical conditions in a TDE. For this, however, detailed modeling of the radiative transfer physics (e.g. Netzer et al. 1985) is required, which is beyond the scope of this paper.

In any case, the detection of prominent Bowen fluorescent lines in TDEs has important implications for the mechanism of emission and the geometry of the emitting gas.

TDEs with Bowen lines should also produce strong EUV or X-ray emission, since a large flux of photons with wavelength shorter than 228 Å is needed to ionize He II and trigger the Bowen mechanism. This flux can not be provided by the blue tail of the UV/optical blackbody continuum that we observe. By integrating a blackbody of 25000 K, we find that only $\sim 10^{-6}$% of the total luminosity is emitted below 228 Å, corresponding to a luminosity of the order of $\sim 10^{36}$ erg s^{-1} (Figure 7). In comparison, the observed Bowen lines have line luminosities of the order of $\sim 10^{41}$ erg s^{-1}, so another ionising source is required.

X-ray/EUV emission in TDEs is usually associated with the accretion process of the transient debris disk (Cannizzo et al. 1990; Ulmer 1999; Lodato & Rossi 2011), since the collisions of debris streams near the apocenter of their orbits will mostly produce optical photons (Piran et al. 2015) unless the star has penetrated very deeply into the tidal disruption radius. In the deep plunge case, however, a prompt formation of an accretion disk is also expected due to efficient orbital energy removal in debris stream collisions (Dai et al. 2015; Guillochon & Ramirez-Ruiz 2015). Therefore, the indirect uncovering of EUV/X-ray photons through the detection of Bowen lines in the optical spectrum, favors the accretion paradigm for optical TDEs.

This unobserved EUV radiation energy component may also (partially) solve the "TDE missing energy problem" (Lu & Kumar 2018) which states that the observed radiation energy in the optical/UV bands for optical TDEs is less than $\sim$ 10% of the rest-mass energy of a star.

EUV radiation is hard to detect due to Galactic extinction. Strong X-rays, however, are also lacking in most optical TDEs with Bowen features except in ASASSN-14li (Miller et al. 2015; Holoien et al. 2016b). This, however, can be a geometric effect as X-ray photons produced by the inner disk are obscured by some gaseous medium such as the unbound debris stream or by winds (Loeb & Ulmer 1997; Strubbe & Quataert 2009; Coughlin & Begelman 2014; Guillochon et al. 2014). Since the debris stream is confined by gravity and therefore has a vertically thin structure (Kochanek 1994; Guillochon et al. 2014), it is unlikely that it will cover a large solid angle. This leaves obscuration by wind as the most likely explanation. It has been proposed that optical TDEs

can be produced by the reprocessing of X-ray photons in optically-thick winds formed in TDEs (Metzger & Stone 2016; Roth et al. 2016). Furthermore, Dai et al. (2018) employed a super-Eddington TDE disk simulation to show that optically-thick winds are indeed produced from such disks. Based on the anisotropic wind profile, a unified picture of X-ray to optical TDEs can be provided by viewing the disk from different inclinations. The optical depth of the super-Eddington disk and wind is large, allowing for multiple scatterings to happen before photons leak out of the system. This can greatly boost the resonance of O III and N III at 304 Å and increase the efficiency of the Bowen mechanism. Most of the radiation energy, indeed, is emitted in the EUV range in this model.

In the electron-scattering dominated regime, the emission lines should be broadened by scattering and therefore the line width is primarily set by the number of scatterings of photons (or the optical depth) instead of gas kinematics (Roth & Kasen 2018). The narrowing of the lines observed in AT 2018dyb (and other TDEs) after peak is consistent with the decrease of optical depth of the system as the debris fallback rate and accretion rate drop with time. In the unified TDE model of Dai et al. (2018), the electron scattering photosphere is larger along the disk direction and tucks in near the pole. This can explain why, between the two TDEs with the strongest Bowen features, ASASSN-14li has narrower lines than AT 2018dyb: ASASSN-14li is viewed through a smaller inclination angle to the pole (consistent with the detection of X-rays), while AT 2018dyb is viewed closer to the disk (higher inclination angle). This makes AT 2018dyb opaque to X-rays while, at the same time, the photons need to go through more scattering to leak out of the photosphere, resulting in broader line profiles.

9. CONCLUSIONS

The main points of this study can be summarized as follows:

- We have unambiguously detected strong lines of N and O in the optical spectra of AT 2018dyb.
- We have shown that these lines are quite common in the spectra of TDEs and that there exist optical TDEs that are 'N-rich'.
- The N III and O III lines are most likely originating from the Bowen fluorescence mechanism.
- The detection of the Bowen lines require the existence of EUV/X-ray photons and this argues for an accretion origin for optical TDEs.
- The strongest emission lines appear slightly blueshifted at early times but progressively move to the red.
- The FWHM of the emission lines decreases with time. This is expected if their width is primarily set by electron scattering (Roth & Kasen 2018) and if the optical depth decreases with time.
- N III starts stronger than He II but He II evolves to become relatively stronger. This is possibly associated with the change of the ionization level.
- These last observations are also valid for ASASSN-14li, which has a spectrum very similar to AT 2018dyb. Two important differences are that the lines of ASASSN-14li are narrower by a factor of $\sim$2 and that it is detected in X-rays.
- These differences can be explained within the unification model of Dai et al. (2018) where TDEs are observed through a super-Eddington disk with an anisotropic optically thick wind. Within this scenario, AT 2018dyb is viewed at a larger polar inclination (closer to the disk mid-plane) than ASASSN-14li and this is why it is opaque to X-rays and why its lines become broader as they go through more scattering on the way out of the photosphere.
- High-resolution spectroscopy of AT 2018dyb obtained close to peak does not reveal any narrow features that can be safely attributed to the TDE (e.g. due to outflows).
- The host galaxy mass is found to be $\log_{10}(M_\star/M_\odot) = 10.08^{+0.25}_{-0.24}$ by SED fitting.
- By using `MOSFiT` we estimate that AT 2018dyb was produced by the disruption of a $0.7^{+4}_{-0.6} M_\odot$ star by a $4^{+5}_{-2} \times 10^6 M_\odot$ black hole.

The observations of AT 2018dyb constitute an excellent dataset that can be used to understand the physical conditions in TDEs through detailed modelling.

We thank Matt Nicholl for comments on the manuscript. GL was supported by a research grant (19054) from VILLUM FONDEN. LD and ER acknowledge the support from DNRF. PGJ, GC and ZKR acknowledge support from European Research Council Consolidator Grant 647208. KM acknowledges support from STFC (ST/M005348/1) and from H2020 through an ERC Starting Grant (758638). MG was supported by the Polish National Science Centre grant OPUS 2015/17/B/ST9/03167. T.-W.C. acknowledges funding from the Alexander von Humboldt Foundation. SJS acknowledges funding from STFC Grants ST/P000312/1 and ST/N002520/1. This work is based on observations collected at the European Organisation for Astronomical Research in the Southern Hemisphere, Chile as part of ePESSTO, (the Public ESO Spectroscopic Survey for Transient Objects Survey) ESO program 199.D-0143. MG is supported by the Polish NCN MAESTRO grant 2014/14/A/ST9/00121.

REFERENCES

Arcavi, I., Gal-Yam, A., Sullivan, M., et al. 2014, ApJ, 793, 38
Arnouts, S., Cristiani, S., Moscardini, L., et al. 1999, MNRAS, 310, 540
Ballester, P., Modigliani, A., Boitquin, O., et al. 2000, The Messenger, 101, 31
Blagorodnova, N., Gezari, S., Hung, T., et al. 2017, ApJ, 844, 46
Blagorodnova, N., Kulkarni, S. B. C. S. R., Arcavi, I., et al. 2018, ArXiv e-prints
Bowen, I. S. 1934, PASP, 46, 146
—. 1935, ApJ, 81, 1
Brimacombe, J., Cornect, R., & Stanek, K. Z. 2018, Transient Name Server Discovery Report, 982

Brown, J. S., Kochanek, C. S., Holoien, T. W.-S., et al. 2018, MNRAS, 473, 1130
Brown, T. M., Baliber, N., Bianco, F. B., et al. 2013, PASP, 125, 1031
Cannizzo, J. K., Lee, H. M., & Goodman, J. 1990, ApJ, 351, 38
Cenko, S. B., Cucchiara, A., Roth, N., et al. 2016, ApJ, 818, L32
Coughlin, E. R., & Begelman, M. C. 2014, ApJ, 781, 82
Crowther, P. A. 2007, Annual Review of Astronomy and Astrophysics, 45, 177
Dai, L., McKinney, J. C., & Miller, M. C. 2015, ApJ, 812, L39
Dai, L., McKinney, J. C., Roth, N., Ramirez-Ruiz, E., & Miller, M. C. 2018, ApJ, 859, L20
French, K. D., Arcavi, I., & Zabludoff, A. 2016, ApJ, 818, L21
Friedman, S. D., York, D. G., McCall, B. J., et al. 2011, ApJ, 727, 33
Gallegos-Garcia, M., Law-Smith, J., & Ramirez-Ruiz, E. 2018, ApJ, 857, 109
Gezari, S., Chornock, R., Rest, A., et al. 2012, Nature, 485, 217
Guillochon, J., Manukian, H., & Ramirez-Ruiz, E. 2014, ApJ, 783, 23
Guillochon, J., Parrent, J., Kelley, L. Z., & Margutti, R. 2017, ApJ, 835, 64
Guillochon, J., & Ramirez-Ruiz, E. 2013, ApJ, 767, 25
—. 2015, ApJ, 809, 166
Holoien, T. W.-S., Prieto, J. L., Bersier, D., et al. 2014, MNRAS, 445, 3263
Holoien, T. W.-S., Kochanek, C. S., Prieto, J. L., et al. 2016a, MNRAS, 463, 3813
—. 2016b, MNRAS, 455, 2918
Holoien, T. W.-S., Huber, M. E., Shappee, B. J., et al. 2018, arXiv e-prints
Hung, T., Gezari, S., Blagorodnova, N., et al. 2017, ApJ, 842, 29
Ilbert, O., Arnouts, S., McCracken, H. J., et al. 2006, A&A, 457, 841
Kallman, T., & McCray, R. 1980, ApJ, 242, 615
Kochanek, C. S. 1994, ApJ, 422, 508
—. 2016a, MNRAS, 458, 127
—. 2016b, MNRAS, 461, 371
Kramida, A., Yu. Ralchenko, Reader, J., & and NIST ASD Team. 2015, NIST Atomic Spectra Database (ver. 5.3), [Online]. Available: `http://physics.nist.gov/asd` [2016, February 23]. National Institute of Standards and Technology, Gaithersburg, MD.
Krühler, T., Greiner, J., Schady, P., et al. 2011, A&A, 534, A108
Leloudas, G., Fraser, M., Stone, N. C., et al. 2016, Nature Astronomy, 1, 0002
Liu, T., Tozzi, P., Wang, J.-X., et al. 2017, ApJS, 232, 8
Liu, X., Dittmann, A., Shen, Y., & Jiang, L. 2018, ApJ, 859, 8
Lodato, G., & Rossi, E. M. 2011, MNRAS, 410, 359
Loeb, A., & Ulmer, A. 1997, ApJ, 489, 573
Lu, W., & Kumar, P. 2018, ApJ, 865, 128
Markwardt, C. B. 2009, in Astronomical Society of the Pacific Conference Series, Vol. 411, Astronomical Data Analysis Software and Systems XVIII, ed. D. A. Bohlender, D. Durand, & P. Dowler, 251
McClintock, J. E., Canizares, C. R., & Tarter, C. B. 1975, ApJ, 198, 641
McConnell, N. J., & Ma, C.-P. 2013, ApJ, 764, 184
Metzger, B. D., & Stone, N. C. 2016, MNRAS, 461, 948
Miller, J. M., & Cenko, B. 2018, The Astronomer's Telegram, 11876
Miller, J. M., Kaastra, J. S., Miller, M. C., et al. 2015, Nature, 526, 542
Mockler, B., Guillochon, J., & Ramirez-Ruiz, E. 2019, ApJ, 872, 151
Netzer, H., Elitzur, M., & Ferland, G. J. 1985, ApJ, 299, 752
Osterbrock, D. E. 1974, Astrophysics of Gaseous Nebulae
Pan, Y. C., Foley, R. J., Jha, S. W., Rest, A., & Scolnic, D. 2018, Transient Name Server Classification Report, 998
Piran, T., Svirski, G., Krolik, J., Cheng, R. M., & Shiokawa, H. 2015, ApJ, 806, 164
Rees, M. J. 1988, Nature, 333, 523
Reines, A. E., & Volonteri, M. 2015, ApJ, 813, 82
Ricci, C., Trakhtenbrot, B., Koss, M. J., et al. 2017, ApJS, 233, 17
Roth, N., & Kasen, D. 2018, ApJ, 855, 54
Roth, N., Kasen, D., Guillochon, J., & Ramirez-Ruiz, E. 2016, ApJ, 827, 3
Schlafly, E. F., & Finkbeiner, D. P. 2011, ApJ, 737, 103
Schulze, S., Krühler, T., Leloudas, G., et al. 2018, MNRAS, 473, 1258
Selvelli, P., Danziger, J., & Bonifacio, P. 2007, A&A, 464, 715
Shappee, B. J., Prieto, J. L., Grupe, D., et al. 2014, ApJ, 788, 48
Smartt, S. J., Valenti, S., Fraser, M., et al. 2015, A&A, 579, A40
Strubbe, L. E., & Quataert, E. 2009, MNRAS, 400, 2070
Tozzi, P., Gilli, R., Mainieri, V., et al. 2006, A&A, 451, 457
Trakhtenbrot, B., Arcavi, I., Ricci, C., et al. 2019, Nature Astronomy
Ulmer, A. 1999, ApJ, 514, 180
Unno, W. 1955, PASJ, 7, 81
Wevers, T., van Velzen, S., Jonker, P. G., et al. 2017, MNRAS, 471, 1694
Weymann, R. J., & Williams, R. E. 1969, ApJ, 157, 1201
Wolf, C., Onken, C. A., Luvaul, L. C., et al. 2018, Publications of the Astronomical Society of Australia, 35, e010
Yaron, O., & Gal-Yam, A. 2012, PASP, 124, 668

Table 1
UVOT photometry of AT 2018dyb [a]

UT (yy-mm-dd)	MJD (days)	Phase [b] (days)	UVW2 (mag)	UVM2 (mag)	UVW1 (mag)	U (mag)	B (mag)	V (mag)
2018-07-18	58317.63	7.3	16.28 (0.07)	16.55 (0.06)	16.25 (0.06)	15.92 (0.05)	15.81 (0.05)	15.59 (0.05)
2018-07-21	58320.65	10.2	16.08 (0.07)	16.38 (0.07)	16.00 (0.06)	15.69 (0.05)	15.65 (0.05)	15.57 (0.06)
2018-07-24	58323.64	13.2	15.97 (0.07)	16.25 (0.06)	15.86 (0.06)	15.61 (0.05)	15.50 (0.05)	15.45 (0.05)
2018-08-04	58334.61	23.9	...	15.91 (0.06)	...	...	...	...
2018-08-06	58336.67	26.0	...	...	...	15.34 (0.05)	...	...
2018-08-09	58339.15	28.4	...	...	15.56 (0.06)	...	...	...
2018-08-19	58349.24	38.3	15.71 (0.07)	15.90 (0.06)	15.62 (0.06)	15.32 (0.05)	15.21 (0.05)	15.17 (0.05)
2018-08-22	58352.09	41.1	15.82 (0.07)	15.91 (0.06)	15.99 (0.06)	15.45 (0.05)	15.37 (0.05)	15.29 (0.06)
2018-08-25	58355.74	44.7	15.83 (0.07)	15.99 (0.06)	15.70 (0.06)	15.45 (0.05)	15.35 (0.05)	15.24 (0.05)
2018-08-31	58361.39	50.3	16.32 (0.07)	16.32 (0.06)	16.03 (0.06)	15.61 (0.05)	15.53 (0.05)	15.37 (0.05)
2018-09-03	58364.28	53.1	16.15 (0.07)	16.19 (0.06)	15.91 (0.06)	15.67 (0.05)	15.52 (0.05)	15.44 (0.05)
2018-09-11	58372.35	61.0	16.32 (0.07)	16.52 (0.06)	16.17 (0.06)	15.98 (0.06)	15.72 (0.05)	15.46 (0.06)
2018-09-14	58375.03	63.7	16.28 (0.07)	16.51 (0.06)	16.22 (0.07)	15.91 (0.06)	15.75 (0.07)	15.55 (0.08)
2018-09-24	58385.61	74.0	16.60 (0.07)	16.84 (0.06)	16.71 (0.06)	16.30 (0.06)	16.04 (0.06)	15.89 (0.07)
2018-09-26	58387.86	76.3	16.76 (0.08)	16.91 (0.07)	16.71 (0.08)	16.41 (0.08)	16.10 (0.09)	15.87 (0.12)
2018-09-29	58390.63	79.0	16.81 (0.08)	17.00 (0.07)	16.76 (0.07)	16.43 (0.07)	16.13 (0.07)	16.00 (0.09)
2018-10-02	58393.71	82.0	16.99 (0.08)	17.09 (0.07)	16.77 (0.07)	16.45 (0.07)	16.26 (0.08)	16.13 (0.11)
2018-10-03	58394.82	83.1	16.86 (0.08)	17.18 (0.08)	16.81 (0.07)	16.49 (0.07)	16.20 (0.07)	15.89 (0.13)
2018-10-15	58406.06	94.1	17.15 (0.07)	17.42 (0.06)	17.10 (0.07)	16.74 (0.06)	16.48 (0.06)	15.95 (0.07)
2018-10-18	58409.63	97.6	17.31 (0.08)	17.61 (0.07)	17.21 (0.07)	16.85 (0.07)	16.54 (0.07)	16.14 (0.08)
2018-10-22	58413.96	101.9	17.44 (0.08)	17.70 (0.07)	17.38 (0.07)	16.97 (0.07)	16.67 (0.07)	16.09 (0.08)
2018-10-26	58417.77	105.6	17.56 (0.08)	17.80 (0.07)	17.42 (0.07)	17.06 (0.07)	16.66 (0.07)	16.41 (0.09)
2018-10-30	58421.85	109.6	17.88 (0.08)	18.10 (0.07)	17.62 (0.07)	17.22 (0.07)	16.83 (0.08)	16.25 (0.09)
2018-11-03	58425.21	112.9	17.78 (0.09)	18.05 (0.08)	17.49 (0.08)	17.23 (0.09)	16.66 (0.09)	16.44 (0.13)
2018-11-06	58428.13	115.8	17.91 (0.08)	18.20 (0.07)	17.66 (0.07)	17.32 (0.08)	16.74 (0.08)	16.17 (0.09)
2019-01-22	58505.04	191.4	18.96 (0.09)	19.18 (0.10)	18.58 (0.09)	18.08 (0.08)	17.27 (0.07)	16.49 (0.07)
2019-01-29	58512.90	199.1	19.10 (0.10)	19.27 (0.10)	18.83 (0.10)	18.10 (0.09)	17.27 (0.08)	16.62 (0.11)
2019-02-02	58516.69	202.8	19.10 (0.10)	19.25 (0.09)	18.77 (0.10)	18.33 (0.10)	17.20 (0.08)	16.55 (0.09)
2019-02-11	58525.20	211.2	19.36 (0.11)	19.46 (0.11)	18.87 (0.10)	18.32 (0.10)	17.48 (0.09)	16.66 (0.10)
2019-02-14	58528.38	214.3	19.43 (0.10)	19.49 (0.09)	19.02 (0.10)	18.28 (0.09)	17.34 (0.08)	16.51 (0.08)
2019-02-18	58532.49	218.4	19.37 (0.10)	19.39 (0.12)	18.85 (0.09)	18.33 (0.09)	17.34 (0.08)	16.58 (0.08)

[a] the magnitudes are given in the AB magnitude system and they are not corrected for Galactic extinction or host galaxy contamination.
[b] with respect to the date of discovery (MJD = 58310.23) and given in the rest frame of AT 2018dyb ($z = 0.0180$).

Table 2
Log of spectroscopic observations

UT (yy-mm-dd)	MJD (days)	Phase [a] (days)	Telescope+instrument	Grism/Grating	Slit width ($''$)	Exposure time (s)
2018-07-19	58318.42	8.0	LCO+FLOYDS	red/blu	2	2700
2018-07-22	58321.22	10.8	VLT+UVES	346+580	1	1800
2018-07-23	58322.21	11.8	VLT+UVES	346+580, 437+860	1	1800, 1800
2018-08-03	58333.11	22.5	NTT+EFOSC2	GR#11, GR#16	1	1500, 1500
2018-08-07	58337.45	26.7	LCO+FLOYDS	red/blu	2	2700
2018-08-13	58343.13	32.3	NTT+EFOSC2	GR#11, GR#16	1	1500, 1500
2018-08-13	58343.47	32.7	LCO+FLOYDS	red/blu	2	2700
2018-08-16	58346.01	35.1	VLT+UVES	346+580, 437+860	1	1800, 1800
2018-08-18	58348.14	37.2	NTT+EFOSC2	GR#11, GR#16	1	1200, 1200
2018-08-28	58358.41	47.3	LCO+FLOYDS	red/blu	2	2700
2018-09-01	58362.98	51.8	NTT+EFOSC2	GR#11, GR#16	1.5, 1	1800, 1800
2018-09-15	58376.03	64.6	NTT+EFOSC2	GR#11, GR#16	1	1800, 1800
2018-09-16	58377.46	66.0	LCO+FLOYDS	red/blu	2	2700
2018-10-02	58393.99	82.3	NTT+EFOSC2	GR#11, GR#16	1	1800, 1800
2018-10-18	58409.00	97.0	NTT+EFOSC2	GR#13	1	1800
2019-01-25	58508.31	194.6	NTT+EFOSC2	GR#13	1	2×1800
2019-02-10	58524.32	210.3	NTT+EFOSC2	GR#11	1	2700
2019-02-25	58539.30	225.0	NTT+EFOSC2	GR#11, GR#16	1	2700, 2700

[a] with respect to the date of discovery (MJD = 58310.23) and given in the rest frame of AT 2018dyb ($z = 0.0180$).